ACS NANO

www.acsnano.org

ARTICLE

Robust Helical Dichroism on Microadditively Manufactured Copper Helices via Photonic Orbital Angular Momentum

Nianwei Dai,[#] Shunli Liu,[#] Zhongguo Ren, Yang Cao, Jincheng Ni, Dawei Wang, Liang Yang, Yanlei Hu, Jiawen Li, Jiaru Chu, and Dong Wu*

Cite This: *ACS Nano* 2023, 17, 1541−1549

Read Online

ACCESS | Metrics & More | Article Recommendations | Supporting Information

ABSTRACT: **Three-dimensional chiral metallic metamaterials have already attracted extensive attention in the wide research fields of chiroptical responses. These artificial chiral micronanostructures, possessing strong chiroptical signals, show huge significance in next-generation photonic devices and chiroptical spectroscopy techniques. However, most of the existing chiral metallic metamaterials are designed for generating chiroptical signals dependent on photonic spin angular momentum (SAM). The chiral metallic metamaterials for generating strong chiroptical responses by photonic orbital angular momentum (OAM) remain unseen. In this work, we fabricate copper microhelices with opposite handedness by additively manufacturing and further examine their OAM-dominated chiroptical response: helical dichroism (HD). The chiral copper microhelices exhibit differential reflection to the opposite OAM states, resulting in a significant HD signal (~50%). The origin of the HD can be theoretically explained by the difference in photocurrent distribution inside copper microhelices under opposite OAM states. Moreover, the additively manufactured copper microhelices possess an excellent microstructural stability under varying annealing temperatures for robust HD responses. Lower material cost and noble-metal-similar optical properties, accompanied with well thermal stability, render the copper microhelices promising metamaterials in advanced chiroptical spectroscopy and photonic OAM engineering.**

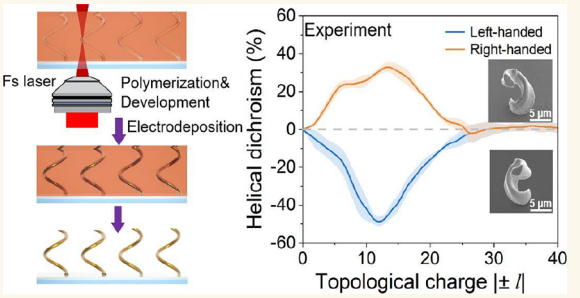

KEYWORDS: *microadditive manufacturing, copper microhelix, vortex beam, orbital angular momentum, helical dichroism, chiroptical response*

1. INTRODUCTION

Three-dimensional (3D) metallic microstructures have attracted considerable interest due to their overwhelming advantages of enhanced light−matter interaction in optical resonant systems.[1−3] Among them, the 3D chiral metallic microstructures have become one of the most important research fields thanks to their giant chiroptical responses.[4−9] It should be noted that the accuracy and reliability of the chiroptical response particularly depend on the formability and surface quality of the 3D chiral metallic microstructures. However, the manufacture of the metallic microstructures at the microscale with higher quality is still considered to be a tough issue. In previous works, various microscale additive manufacturing technologies, such as electrohydrodynamic (EHD) printing,[10] meniscus-confined electroplating (MCE),[11,12] electroplating of locally dispensed ions in liquid,[13] laser-assisted electrophoretic deposition (LAEP),[14] laser-induced forward transfer (LIFT),[15,16] and laser-induced photoreduction,[10,17,18] have been successively developed to fabricate the 3D metallic microstructures. Nevertheless, the 3D metallic microstructures manufactured through the above-mentioned methods are normally defective and rough due to the existence of residual organic constituents and surfactant molecules inside the as-deposited structures. The addition of organic surfactants and the associated suppression of the grain growth result in an agglomeration of deposited nanoparticles, consequently failing to meet the preparation requirements of 3D chiral metallic microstructures. Therefore, the surface

Received: October 26, 2022
Accepted: January 9, 2023
Published: January 11, 2023

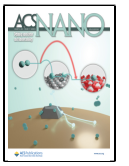

Downloaded via UNIV SCIENCE AND TECHNOLOGY CHINA on March 6, 2023 at 09:44:24 (UTC).
See https://pubs.acs.org/sharingguidelines for options on how to legitimately share published articles.

ACS Publications

© 2023 American Chemical Society

https://doi.org/10.1021/acsnano.2c10687
ACS Nano 2023, 17, 1541−1549

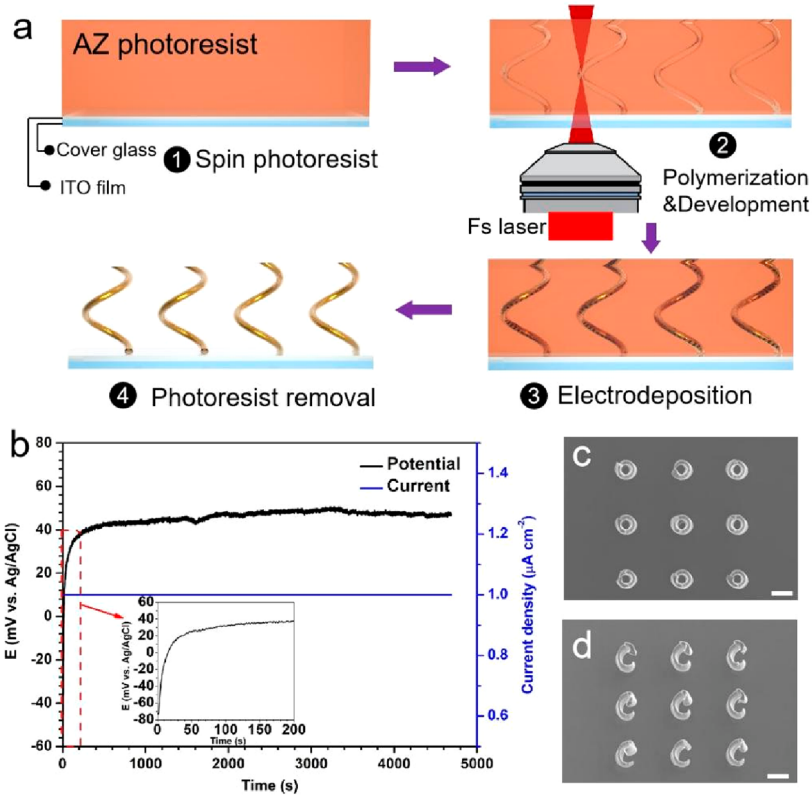

Figure 1. Microadditive manufacturing of 3D copper microhelices by femtosecond laser writing and electrodeposition. (a) The microhelix structures were written inside the AZ9260 positive-tone photoresist by femtosecond laser direct writing, followed by electroplating in acidic $CuSO_4$ solution, and was finally developed in developer to obtain the desired helical copper microstructures. (b) The chronopotentiometry method based on a three-electrode system was employed to perform the electrodeposition process. A constant current was applied on ITO electrode, and the potential underwent an obvious positive shift from a negative potential. (c, d) SEM images of representative copper microhelices from the top view and tilted view. Scale bars, 10 μm.

quality of as-manufactured microstructures strictly depends on appropriate postannealing treatments.[10,14,16−19]

In virtue of the above reasons, the template-assisted electrodeposition method was then proposed to additively manufacture metallic microstructures with satisfactory surface quality. Metallic microstructures like gold helices,[20] copper meso-lattices,[21] and hybrid helical magnetic microrobots[22] have been successfully fabricated, and the corresponding surface quality can be controlled through optimization of the electrodeposition parameters. As for the template-assisted method, the electrodeposition of noble metals rigorously depends on the complicated plating solution systems and strict parameters, causing the electroplating a high-cost and uncontrollable processing. Copper, widely used in electronics and microelectro-mechanical systems, possesses a close dielectric constant with gold and silver materials in common optical wavelengths, which can be potentially used as an alternative optical material to the noble metals. In comparison with electrodeposition of noble metals, copper microstructures with ideal surface quality can be electrodeposited with a simple acidic plating solution and the electrodeposition parameters are relatively easy to be ascertained. Also, the electrodeposited copper with a relatively smooth surface generally possesses an excellent antioxidation degradation property in common environments.[23] All these spur the chiral copper microstructures potential substitutes in next-generation chiroptical spectroscopy techniques.

As for the chiroptical response,[24] it can be understood as the external manifestation of the chiral micro/nanostructures and chiral light waves in the light−matter interaction at the microscopic scale. For chiral light waves, the most famous ones are circularly polarized lights carrying spin angular momentum (SAM) and vortex beams carrying orbit angular momentum (OAM).[25,26] As is well-known, the chiral 3D metallic microstructure enables differential transmission of two circularly polarized lights (essentially photonic SAM) in opposite states.[27−30] As a dimension alongside SAM, photonic OAM of vortex beams has gradually attracted attention in the study of chiral optics.[31−36] Metallic microhelices are promising in the study of photonic OAM-dependent chiroptical phenomena due to their enhanced light−matter interactions of spatial 3D features. Therefore, exploring the interaction between metallic chiral structures and photonic OAMs is of great significance for expanding the photonic dimensions of chiroptical phenomena. Furthermore, when the 3D metallic chiral microstructures are employed in the advanced chiroptical spectroscopy technique, it is highly possible that the chiroptical devices could experience elevated temperatures (i.e., up to 400 °C).[37] In virtue of this reason, the stability of 3D metallic microstructures in structures and chiroptical responses at higher temperatures is worthy of being further expounded.

Here, the helical dichroism (HD) of copper microhelices was experimentally investigated and theoretically analyzed. We prepared 3D copper microhelices through the template-

https://doi.org/10.1021/acsnano.2c10687
ACS Nano 2023, 17, 1541−1549

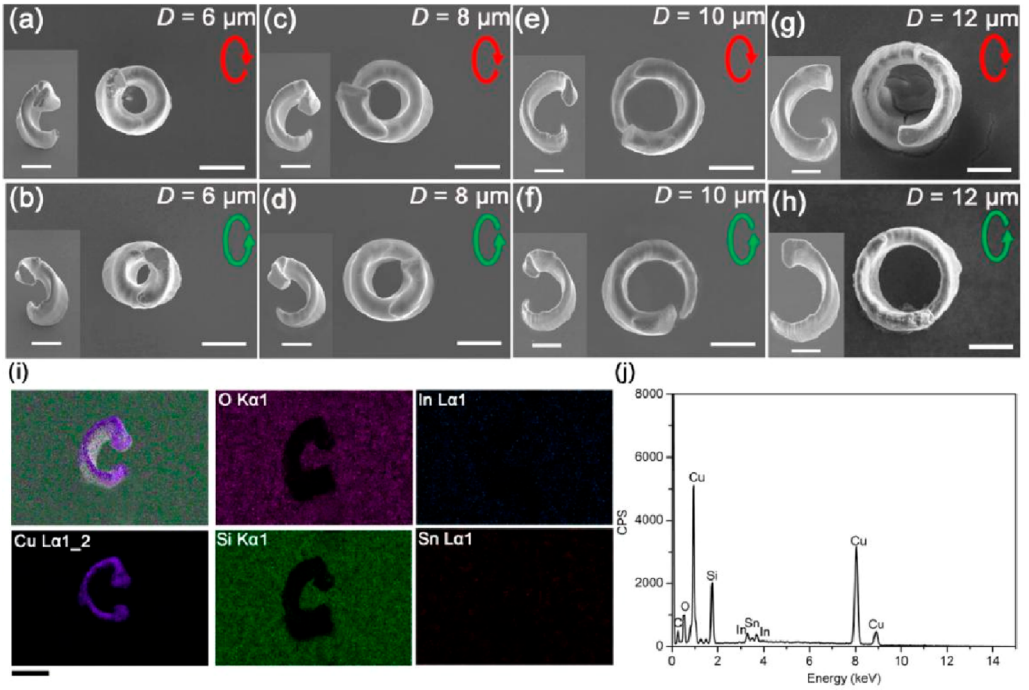

Figure 2. Characterization of copper microhelices with varied diameters. (a–h) SEM images of microadditively manufactured left- and right-handed copper helices with varied diameters from 6 to 12 μm and the same helical pitch of h = 16 μm. The insets are images with a 30° tilted view. Scale bars, 5 μm. (i) The major element mapping of an 8 μm copper microhelix from a tilted view. Scale bar, 5 μm. (j) The chemical composition of major elements for the copper microhelix characterized by energy-dispersive X-ray spectroscopy (EDS).

assisted electrodeposition and experimentally measured the vortex-dependent HD spectra of the corresponding copper microhelices with opposite handedness. The experimental results of reflectance spectra and HD spectra on the single copper microhelix agree well with the simulation results. In addition, the regular HD spectra for copper microhelices with varied diameters and the thermal stability of microhelices under different temperatures were further examined, showing the robustness of HD spectra. The copper microhelices may find applications in the chiral metamaterial design and advanced chiroptical sensing.

2. RESULTS AND DISCUSSION

2.1. Additive Manufacturing of Copper Microhelices by Combining Femtosecond Laser Direct Writing with Electrodeposition. A hybrid method combining femtosecond laser direct writing in the positive-tone photoresist with successive electrodeposition is employed to microadditively manufacture copper helices. As shown in Figure 1a, a positive-tone photoresist AZ9260 was spin-coated on ITO glasses with a thickness of 20 μm. Then, the arrays of left- and right-handed microhelices were directly written inside the photoresist by the femtosecond laser direct writing technique. The detailed parameters of designed microhelices can be seen in Figure S1. The ITO samples with the helical microstructures inside were then developed in developer AZ 400K for enough time to remove the laser-scanned portion, finally forming helical microchannels inside the photoresist. After that, the ITO samples were used as working electrodes to perform the electrodeposition in acidic $CuSO_4$ solution. It should be noted that the chronopotentiometry method was employed to electrodeposit copper microhelices with dense structures. Figure 1b shows the variation of potential with time under the galvanostatic model (constant current density of 1 μA·cm^{-2}). It can be found that the electrode potential exhibits a positive shift from −73.3 to 42 mV, suggesting that the reduction of Cu^{2+} occurs and Cu crystals additively accumulate along the microhelix channels. The usage of a lower current density during the electrodeposition processing is instrumental in forming dense microstructures without distinct defects. Finally, the ITO samples were immersed in acetone to remove the unprocessed photoresist, leaving the desired copper microhelices (see the Experimental Section for more details). Figure 1c,d presents the top view and tilted view for the array of 8 μm left-handed copper microhelices after removing excessive photoresists.

Figure 2a–h presents the SEM images of copper microhelices with varied diameters from 6 to 12 μm and the same helical pitch of h = 16 μm. From the top view and tilted view (inset figures) of the copper microhelices, it can be seen that the microhelix surface is relatively smooth and without obvious defects, which can be ascribed to the advantage of low-current (1 μA·cm^{-2}) electrodeposition in our experiments. Herein, it should be noted that the wire diameter of the copper microhelix is larger than the designed size of 2 μm (as shown in Figure S1). As a matter of fact, the edge of the laser spot also carries a specific power, and the excessive photoresists would be processed during the femtosecond laser direct writing. Also, the excessive photoresists could be removed during the developing process, leading to a path diameter slightly larger than 2 μm. In addition, the deposited copper microstructure contains a strain that possibly enlarges the microhelix diameter during the electrodeposition process. All three aspects finally cause a larger path diameter than the designed one. In order to characterize the elemental composition of the microhelix, we further performed the analysis of element mapping of the microhelix. As shown in Figure 2i, it can be observed that the element mapping of Cu

https://doi.org/10.1021/acsnano.2c10687
ACS Nano 2023, 17, 1541−1549

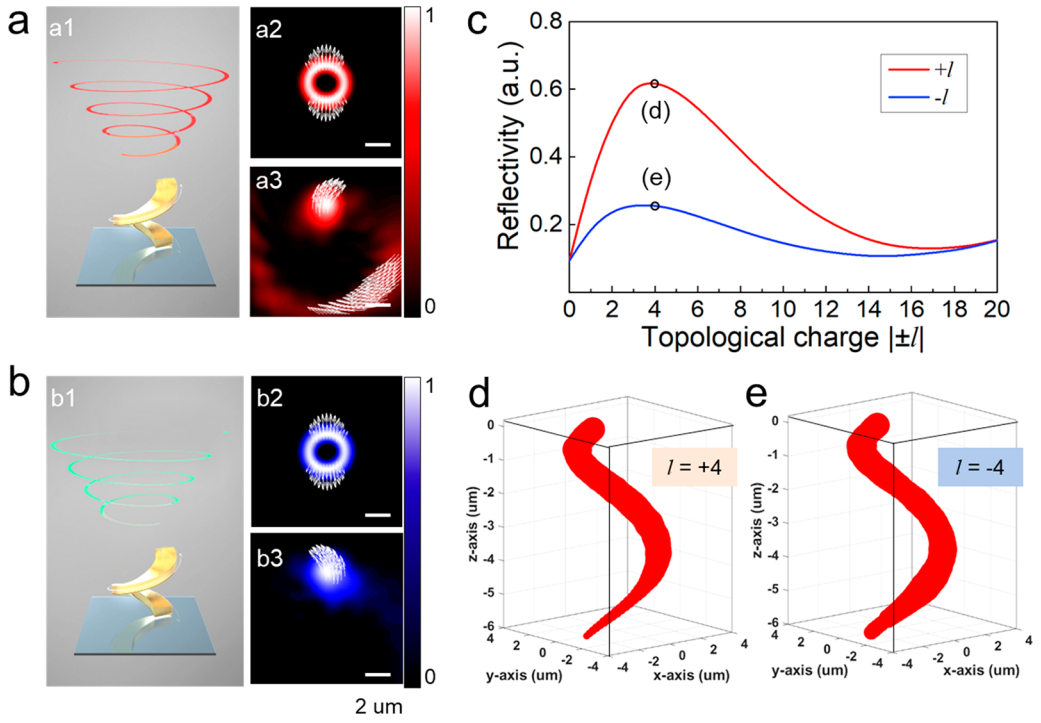

Figure 3. Simulation of HD of the single copper microhelix. (a) (a1) Schematic illustration of a left-handed microhelix illuminated by the vortex beam with topological charge $l = 4$. (a2) The original electric field and Poynting vector (white arrows) distribution of the vortex beam with $l = 4$. (a3) Electric field distribution on the reflection monitoring plane. (b) The left-handed microhelix illuminated by the vortex beam with topological charge $l = -4$. (c) Simulated reflectivity as a function of topological charge l of vortex beams for the left-handed microhelix. (d, e) Photocurrent distribution on the microhelix with topological charges of $l = 4$ (d) and $l = -4$ (e), respectively.

exhibits a helix shape, suggesting that the composition of the 3D microhelix is basically copper (>90 wt %). The elements O, Si, In, and Sn are also displayed in the mapping, which mainly come from the ITO glass. Furthermore, the energy-dispersive X-ray spectroscopy (EDS) in Figure 2j verifies the high proportion of Cu elements in the microhelix.

2.2. Theoretical Simulation of HD of the 3D Copper Microhelix. The chiral metallic micro/nanostructures have a wide range of applications in the field of chiral photonics, manifesting in their asymmetric transmission modulation to chiral beams. The vortex beam is a typical chiral beam owing to the photonic OAM it carries. Here, we theoretically demonstrate the feasibility of manufactured copper microhelices for the transmission manipulation of opposite-mode vortex beams. By means of finite-difference time-domain (FDTD) software, we simulated the interaction process of the left-handed chiral metamaterial with the vortex beams of opposite modes, as shown in Figure 3. Taking into account the computational time, we simulated the chiral copper helix with a diameter of 4 μm and pitch of 6 μm. The OAM modes of the incident vortex beams are selected as $l = 4$ and -4, whose polarization states are set to be linearly polarized along the x direction. For the incident OAM mode of $l = 4$ (a1), its original electric field distribution is a perfect ring with an outward Poynting vector (a2). After interacting with the left-handed copper microhelix, the electric field distribution of the reflection monitoring plane is no longer annular, and the Poynting vector changes from outward to counterclockwise (a3). While for the incident mode of $l = -4$ (b1), a different result will be produced compared with $l = 4$. On the incident plane of the light source, the electric field and Poynting vector distribution of the vortex beam of $l = -4$ are the same as those of $l = -4$ (b2). However, after the interaction with the copper microhelix, the electric field intensity of the reflecting plane is attenuated more severely, and the Poynting vector also changes from outward to clockwise.

Further, when the OAM mode of the vortex beam changes continuously, the differential reflectance spectrum of the left-handed metallic microhelix can be obtained, as shown in Figure 3c. It can be seen that, in the range of $|l|$ from 0 to 20, the reflectivity of the left-handed copper microstructure for the positive OAM mode is always stronger than that of the negative one. This phenomenon of asymmetric transmission of vortex beams by chiral structures is defined as HD. To reveal the origin of HD, we calculated the photocurrent intensity along the chiral microhelix under opposite OAM modes of $l = 4$ (Figure 3d) and $l = -4$ (Figure 3e). The photocurrent intensity distributions are basically the same in the upper half of the microhelix, while the photocurrent intensity of $l = 4$ is weaker than that of $l = -4$ in the lower half of the microhelix. It means that, when the mode of the incident vortex beam is $l = -4$, the interaction between the light and the copper microhelix is more intense, resulting in greater absorption and weakened reflection intensity than that of $l = 4$.

2.3. Vortex-Dependent Reflectance and HD Spectra of 3D Copper Microhelices. To verify the simulation predictions, we measured the vortex-dependent reflectance spectra of a single chiral copper microhelix through the home-built optical system in Figure 4. Taking the topological charge of the vortex beam as an independent variable, we measured the experimental and simulated reflectance spectra of the copper microhelix with a diameter of 6 μm and a pitch of 16 μm. For the right-handed copper microhelix, it exhibits a stronger reflection for $+l$ than for $-l$ in the range from 3 to 25,

https://doi.org/10.1021/acsnano.2c10687
ACS Nano 2023, 17, 1541−1549

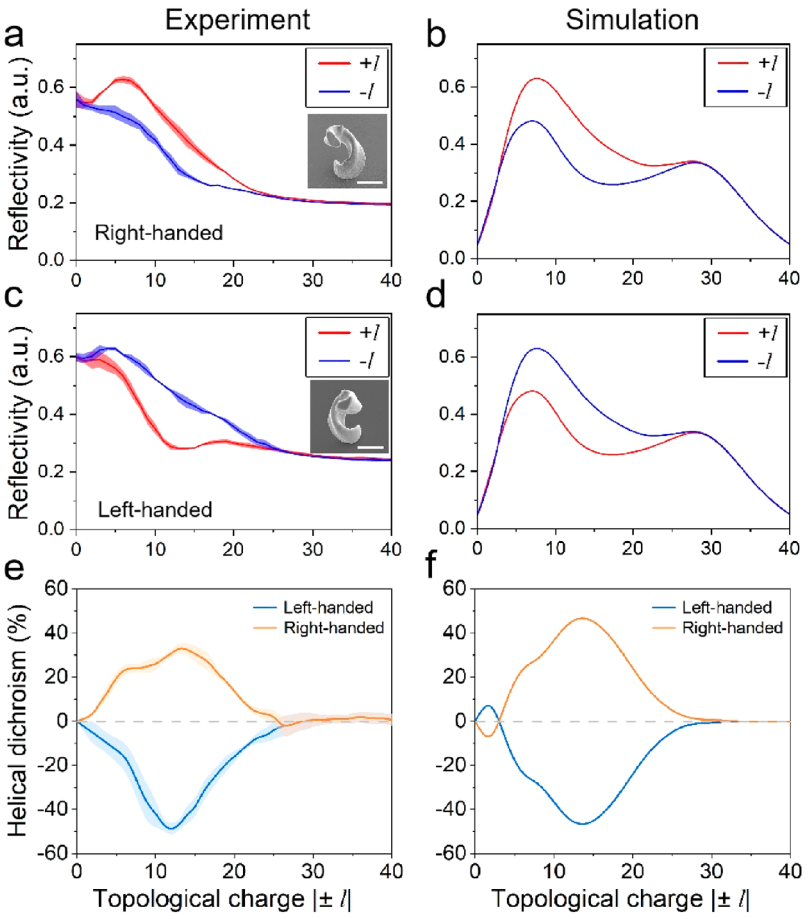

Figure 4. Vortex-dependent reflectance and HD spectra of the single copper microhelix. (a–d) Measured and simulated reflectance on right-handed (a, b) and left-handed (c, d) copper microhelices by vortex beams with topological charge |±*l*| from 0 to 40. The insets are representative right- and left-handed copper microhelices. Scale bars, 5 μm. (e, f) Measured (e) and simulated (f) HD spectra of copper microhelices by vortex beams.

as shown in Figure 4a. We attribute the absence of reflection differences in the other |*l*| ranges to the mismatch of chiral microhelix and the diameter of the vortex beam.[34] In contrast, the reflectance spectra are entirely inversed for the left-handed copper microhelix (Figure 4c). Similarly, we calculated the vortex-dependent reflectance spectra of chiral microhelices with the same diameters of microadditively manufactured copper microhelices based on the full electromagnetic FDTD method. As shown in Figure 4b,d, the simulated reflectance spectra have a similar trend to the measured reflectance spectra, especially in the resonant range of $|l| \in (3, 25)$. Meanwhile, it should also be noted that the simulated reflectance spectra exhibit obviously lower values than the experiment with topological charge |*l*| in the off-resonance ranges of $|l| \in (0, 5)$ and $|l| \in (30, 40)$. The difference between simulation and experiment is mainly ascribed to the inhomogeneous geometrical line width, surface condition, and the uncertainty of optical measurements.

The HD of the copper microhelices is also calculated to further elucidate the OAM-dependent chiroptical phenomena on a single copper microhelix. The definition of HD index refers to the g-factor in circular dichroism

$$\mathrm{HD}\ (\%) = \frac{R^{+l} - R^{-l}}{(R^{+l} + R^{-l})/2} \times 100\% \qquad (1)$$

where R represents the reflectance and its superscript is the topological charge l. According to the formula, the experimental HD spectrum of copper microhelix with a diameter of 6 μm is displayed as shown in Figure 4e. As for the right-handed microhelix, the HD spectrum exhibits a positive value and a local peak can be observed at the topological charge $|\pm l| = 15$. On the contrary, the HD value is negative for the left-handed copper microhelix, suggesting an obvious chiroptical response. However, the HD peak for the negative branch appears at the topological charge $|\pm l| = 13$. Furthermore, the maximum HD signal of ~30% is obtained on the right-handed copper microhelix at the wavelength of 800 nm, while the corresponding value is 50% for the left-handed one. In terms of the simulated HD spectrum (Figure 4f), the chiroptical response of the positive and negative branches is still apparent. However, the difference is that the maximum HD signal for the positive branch is 45%, which is higher than that of the experimental result. Moreover, it should also be noted that the difference between the experimental results and the simulation results for the vortex-dependent reflectance and HD spectrum of the single copper microhelix is relatively large, when the topological charge is smaller than 8. This can be explained by the following reasons: (a) The actual structure does not fit the ideal microspiral model in the simulation very well, and there is always a certain processing error in actual processing. (b) The experimental vortex beam cannot achieve

https://doi.org/10.1021/acsnano.2c10687
ACS Nano 2023, 17, 1541–1549

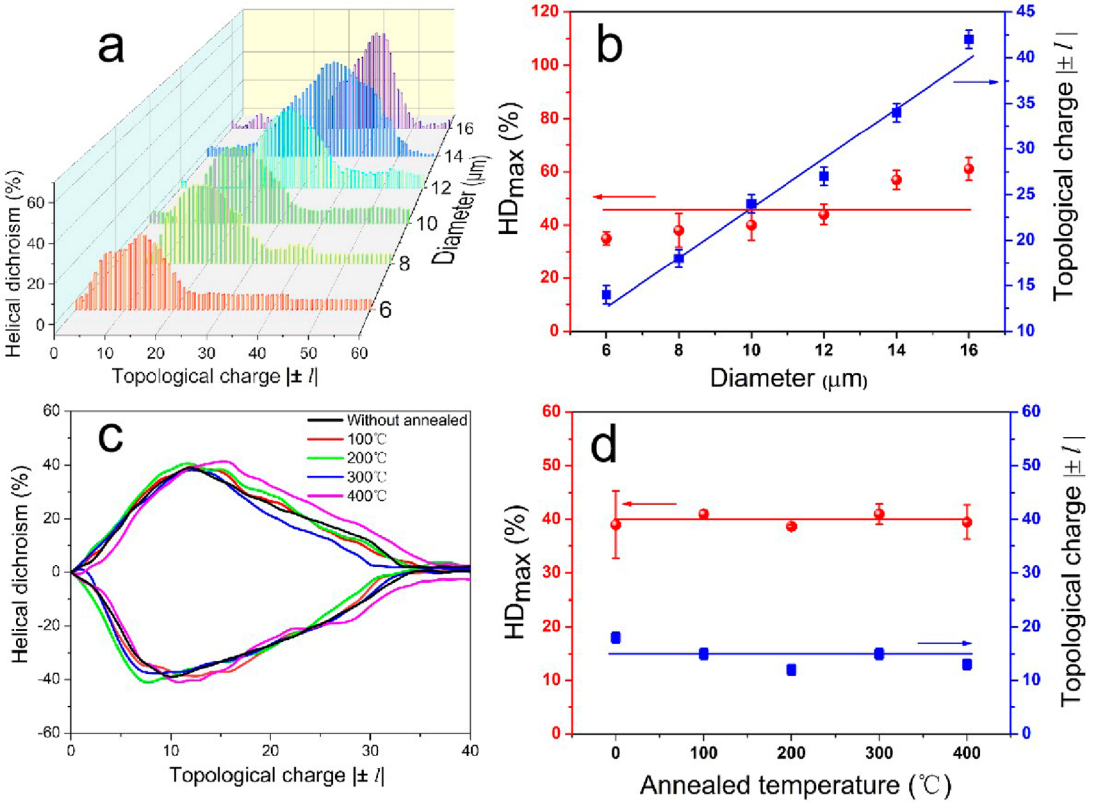

Figure 5. Robust thermal stability of the copper microhelix HD phenomena. (a) Measured HD spectra of copper microhelices with varied diameters from 6 to 16 μm. (b) Maximum value of HD spectra and corresponding topological charge $|\pm l|$ for copper microhelices with varied diameters. (c) HD spectra of copper microhelices after heat treatments with different temperatures from 100 to 400 °C. (d) The maximum value of HD and corresponding topological charge $|\pm l|$.

the perfect light intensity distribution of the vortex beam in the simulation; especially when the number of topological charges is relatively small (l < 10), the experimental vortex light is prone to a certain degree of distortion, which will bring errors in this interval (l < 10). More details on the experimental HD spectra of copper microhelices with diameters from 8 to 12 μm can be found in Figure S2. According to the HD spectra in Figure S2, the right- and left-handed copper microhelices with varied diameters all exhibit apparent chiroptical responses. The detailed information on the variation of the maximum HD value and corresponding topological charge $|\pm l|$ will be further discussed in the next section.

2.4. Robust Thermal Stability of the Copper Microhelix HD Phenomena. Since the HD phenomenon relies on the resonance coupling between the copper microhelix and vortex electric field distribution, the diameter of the metallic microhelix is the most important factor affecting the trend of the HD spectra. The experimental HD spectra of right-handed copper microhelices with varied diameters from 6 to 16 μm are also shown in Figure 5a to further investigate the effect of helix diameter on the HD signals. Figure 5b plots the variation of the maximum HD value and corresponding topological charge $|\pm l|$ with diameters of copper microhelices. The dispersion range of the maximum HD values for copper microhelices with varied diameters is relatively narrow. However, the corresponding topological charge $|\pm l|$ to the HD peaks exhibits a rigorous linear relationship with diameters of copper microhelices.

Regarding the promising application of microadditively manufactured copper helices in electronics and sensors as chiroptical devices, unexpected failure of helix microstructures in a system caused by the elevated temperature is considered to be a tough challenge in corresponding environments in which any microstructural changes could interfere with the chiroptical responses. As such, we also investigated the thermal stability of additively manufactured copper microhelices at high temperatures, as well as the chiroptical response characteristics. The additively manufactured copper microhelices are annealed at 100, 200, 300, or 400 °C, respectively, for 1 h in Argon gas flow. According to the microstructural characteristics of annealed copper microhelices, no obvious changes on the surface morphology and helix shape can be observed, suggesting that the copper microhelix possesses a well thermal stability and even experiences a relatively low-temperature annealing (see Figure S3). As a matter of fact, the copper microstructures additively manufactured by electrodeposition will not be deformed or degraded until the annealed temperature increases to 450 °C.[37]

As shown in Figure 5c, the experimental HD spectra of right- and left-handed copper microhelices annealed with varied temperatures from 100 to 400 °C are plotted and almost all the HD spectra overlapped. The largest HD_{max} variation ($|\Delta HD_{max}|$) and the largest shift of topological charge ($|\Delta l|$) for copper microhelices annealed from 100 to 400 °C are only 3% and 5, respectively, suggesting a stable chiroptical response under the thermal annealing with elevated temperatures. In comparison, the thermal stability of microhelices manufactured with a negative-tone photoresist by femtosecond laser two-photon polymerization is also examined, as can be seen in Figure S4. The photoresist-made microhelices deform once the annealing temperature increases to 300 °C and the higher

https://doi.org/10.1021/acsnano.2c10687
ACS Nano 2023, 17, 1541−1549

temperature of 400 °C consequently induces the severe deformation. It is also observed that the organic microhelices experience an obvious shrinking trend after being annealed with increasing temperatures. As can be seen in Figure S4i, the maximum value of HD spectra for microhelices annealed with elevated temperatures also exhibits an apparent attenuation. The largest HD_{max} variation ($|\Delta HD_{max}|$) for organic microhelices annealed from 100 to 400 °C is up to 34% compared with the as-manufactured one, which is evidently higher than that of copper microhelices. This suggests that the chiroptical response of organic microhelices is susceptible to deformation of microhelices due to the thermal effect. Even the largest value of $|\Delta HD_{max}|$ for organic microhelices is evidently higher than that of copper microhelices, and the decay of HD_{max} under varying annealing temperatures would negatively impact its stable service as the chiroptical detection technology.

3. CONCLUSION

In summary, copper microhelices with varied diameters are additively manufactured by the template-assisted electrodeposition. As an optical application, the experimental observation of chiroptical responses on a single copper microhelix by the photonic OAM of vortex beams has been demonstrated. Nearly symmetric HD spectra can be obtained on right-handed and left-handed copper microhelices, and the maximum HD signal can reach ∼50%. Theoretical analysis based on the FDTD simulation supports the experimental results of the OAM-dependent chiroptical responses. Furthermore, the additively manufactured copper microhelices annealed at elevated temperatures also exhibit an excellent stability in microstructures and chiroptical responses. The achievement of effective and stable chiroptical responses on a non-noble metal, copper microhelix is actually of great significance in photonic angular momentum engineering and the potential application of the next-generation chiroptical spectroscopy.

4. EXPERIMENTAL SECTION

4.1. Additive Manufacturing of Chiral Copper Microhelices. The additive manufacturing of copper microhelix was achieved through the electrodeposition in an ITO template with a microhelix path. First of all, a 50 nm thick layer of indium−tin oxide (ITO) was sputtered onto a glass cover to build a conductive surface. The positive-tone photoresist AZ9260 (Merck, America) with a thickness of 20 μm, acting as the template, was spin coated onto the ITO slide with a spin coater (SM-150, Japan). The spin-coating process consists of two steps: one was done at 2400 rpm for 60 s followed by a 4 min-soft bake at 110 °C. To obtain the desired thickness, the second step was spin coated at 2100 rpm for 60 s and 12 min of soft bake at 110 °C. The femtosecond laser was employed to create the template for the microhelices. The microhelix structures were written vertically with a 60× magnification objective through immersion oil (IMMOIL-8CC) into the photoresist by using a laser power of 10 mW with a single-point exposure time of 1000 μs. After the exposure, the specimen with the microstructures was developed for 30 min in AZ400K developer and cleaned in distilled water for 15 min. Subsequently, the ITO samples were connected with the conductive wire to prepare the working electrodes. After that, the electrodeposition was performed by using a three-electrode system with an Ag/AgCl reference electrode and a Pt counter electrode. The electrolyte for electrodeposition was the simple acidic copper sulfate, which consists of 125 g/L $CuSO_4{\cdot}5H_2O$ and 50 g/L H_2SO_4. The electrodeposition process was conducted by a Donghua 7001 workstation and performed in a galvanostatic mode with a current density of 1 $\mu A{\cdot}cm^{-2}$. The electroplating solution was constantly stirred and maintained at 40 °C during the deposition. The sample was then taken out and immersed in acetone for 2 min to remove the excessive photoresists, followed by cleaning in ethanol and distilled water. To avoid the oxidization, the ITO specimen with helix microstructures was kept in a vacuum dryer.

4.2. Characterization of Copper Microhelices. The microstructures of the additively manufactured copper microhelices were characterized by using cold field emission scanning electron microscopy (FESEM, Hitachi, SU8220), and the elemental analysis was performed through an energy dispersive spectrometer (EDS, Oxford, X-Max80).

4.3. OAM-Dependent Reflection Spectroscopy Measurements of Single Chiral Copper Microhelix. A mode-locked Ti:sapphire ultrafast oscillator (Chameleon Vision-S, Coherent, Inc.) was employed as the femtosecond laser source. The central wavelength of the laser was 800 nm with a pulse width of 75 fs and a repetition rate of 80 MHz. The phase-only reflective liquid-crystal SLM (Pluto NIR-2, Holoeye Photonics AG) has 1920 × 1080 pixels with a pixel pitch of 8 μm on which computer-generated holograms with 256 gray levels can be displayed. A general 100× dry objective lens (NA = 0.9, Olympus) was used in chiroptical detection. The sample was fixed on a 3D-piezo-nanostage (E545, Physik Instrumente) with nanoscale resolution and a 200 μm × 200 μm × 200 μm traveling range to precisely tune the locations of the copper microhelix under optical microscopy. The white light in microscopy was used for observing the precise position of the copper microhelix, which was switched off in reflectance measurements. The vortex beams with tailored topological charges were focused on the copper microhelices at normal incidence by the microscope objective.

The right- and left-handed copper microhelices are precisely positioned for aligning to the generated vortex beam through the 3D-piezo-nanostage. After positioning the microhelix to the beam axes of optical vortices, the reflected intensity was caught utilizing a CCD (MindVision HD-SUA133GM-T camera; image area: 1280 × 1024 pixels) with the acquisition time of 30 ms. The laser power of incident vortex beams was 0.5 mW for achieving clarified optical images on the CCD.

4.4. Numerical Simulation. The numerical simulations were performed by a commercial finite difference time-domain-based software (Lumerical FDTD Solutions, Inc.). In the simulation, the background index of refraction was set to 1.0, and the refractive index of the copper microhelix was set up as a built-in model "Cu (Copper) - CRC" in the software. At the measurement wavelength of 800 nm, the index of refraction corresponding to the copper microhelix is 0.250431 + i × 5.06179. Perfectly matched layer boundaries were employed for the X, Y, and Z directions, and the grid spacing is set to 50 nm for trading off the simulation time and accuracy. The incident linearly polarized vortex beam electric field $E^l(r,\phi)$ is imported via a scripting language as

$$E^l(r,\phi) = \frac{C}{\sqrt{|l|!}} r^{|l|} \exp\left(-\frac{r^2}{\omega_0{}^2}\right) \exp(il\phi)\hat{x} \tag{2}$$

where C denotes a normalized constant, ω_0 means the beam waist based on the experimental system, $\hat{x}$ represents the polarization direction, l is the topological charge of the incident vortex beam, and (r,ϕ) is the polar coordinate system. The distance between the light source plane and the top of the copper microhelix is greater than one wavelength, and the reflection detection plane is located 2 μm above the light source plane.

ASSOCIATED CONTENT

Supporting Information

The Supporting Information is available free of charge at https://pubs.acs.org/doi/10.1021/acsnano.2c10687.

Illustration of the designed right- and left-handed microhelices; experimental HD spectra of copper microhelices; SEM images of additively manufactured

https://doi.org/10.1021/acsnano.2c10687
ACS Nano 2023, 17, 1541−1549

copper microhelices; thermal stability of microhelices (PDF).

AUTHOR INFORMATION

Corresponding Author

Dong Wu − *CAS Key Laboratory of Mechanical Behavior and Design of Materials, Department of Precision Machinery and Precision Instrumentation, University of Science and Technology of China, Hefei, Anhui 230027, China;* orcid.org/0000-0003-0623-1515; Email: dongwu@ustc.edu.cn

Authors

Nianwei Dai − *CAS Key Laboratory of Mechanical Behavior and Design of Materials, Department of Precision Machinery and Precision Instrumentation, University of Science and Technology of China, Hefei, Anhui 230027, China*

Shunli Liu − *CAS Key Laboratory of Mechanical Behavior and Design of Materials, Department of Precision Machinery and Precision Instrumentation, University of Science and Technology of China, Hefei, Anhui 230027, China*

Zhongguo Ren − *CAS Key Laboratory of Mechanical Behavior and Design of Materials, Department of Precision Machinery and Precision Instrumentation, University of Science and Technology of China, Hefei, Anhui 230027, China*

Yang Cao − *CAS Key Laboratory of Mechanical Behavior and Design of Materials, Department of Precision Machinery and Precision Instrumentation, University of Science and Technology of China, Hefei, Anhui 230027, China*

Jincheng Ni − *CAS Key Laboratory of Mechanical Behavior and Design of Materials, Department of Precision Machinery and Precision Instrumentation, University of Science and Technology of China, Hefei, Anhui 230027, China; Department of Electrical and Computer Engineering, National University of Singapore, Singapore 117583, Singapore;* orcid.org/0000-0001-9308-4511

Dawei Wang − *CAS Key Laboratory of Mechanical Behavior and Design of Materials, Department of Precision Machinery and Precision Instrumentation, University of Science and Technology of China, Hefei, Anhui 230027, China*

Liang Yang − *CAS Key Laboratory of Mechanical Behavior and Design of Materials, Department of Precision Machinery and Precision Instrumentation, University of Science and Technology of China, Hefei, Anhui 230027, China; Institute of Nanotechnology, Karlsruhe Institute of Technology (KIT), Karlsruhe 76128, Germany*

Yanlei Hu − *CAS Key Laboratory of Mechanical Behavior and Design of Materials, Department of Precision Machinery and Precision Instrumentation, University of Science and Technology of China, Hefei, Anhui 230027, China;* orcid.org/0000-0003-1964-0043

Jiawen Li − *CAS Key Laboratory of Mechanical Behavior and Design of Materials, Department of Precision Machinery and Precision Instrumentation, University of Science and Technology of China, Hefei, Anhui 230027, China;* orcid.org/0000-0003-3950-6212

Jiaru Chu − *CAS Key Laboratory of Mechanical Behavior and Design of Materials, Department of Precision Machinery and Precision Instrumentation, University of Science and Technology of China, Hefei, Anhui 230027, China;* orcid.org/0000-0001-6472-8103

Complete contact information is available at: https://pubs.acs.org/10.1021/acsnano.2c10687

Author Contributions

[#]N.D. and S.L. contributed equally to this work. J.N. and D.Wu conceived the idea and developed the theory. S.L. performed the simulations. N.D., Z.R., Y.C., and D.Wang performed the experiments. N.D., S.L., J.N., Y.H., J.L., and D.Wu analyzed the data. N.D. and S.L. wrote the manuscript. L.Y., D.Wu, and J.C. supervised the project. All authors discussed the results and commented on the manuscript.

Notes

The authors declare no competing financial interest.

ACKNOWLEDGMENTS

This work was supported by the National Natural Science Foundation of China (Grant Nos. 61927814, 52122511, 91963127, 52075516, 51875544, and U20A20290), Major Scientific and Technological Projects in Anhui Province (201903a05020005), and the Open Project Program of Wuhan National Laboratory for Optoelectronics (No. 2019WNL0KF014), Open Research Fund of Advanced Laser Technology Laboratory of Anhui Province (No. AHL2020KF01), the University Synergy Innovation Program of Anhui Province (GXXT-2021-027), and the Fundamental Research Funds for the Central Universities (WK5290000003). This work was also financially supported by the China Postdoctoral Science Foundation (No. 2021M693043). We acknowledge the Experimental Center of Engineering and Material Sciences at USTC for the fabrication and measuring of samples. This work was partly carried out at the USTC Center for Micro and Nanoscale Research and Fabrication.

REFERENCES

(1) Huang, Y.; Fang, Y.; Zhang, Z.; Zhu, L.; Sun, M. Nanowire-supported plasmonic waveguide for remote excitation of surface-enhanced Raman scattering. *Light Sci. Appl.* **2014**, *3*, e199−e199.

(2) Yokota, Y.; Ueno, K.; Misawa, H. Highly controlled surface-enhanced Raman scattering chips using nanoengineered gold blocks. *Small* **2011**, *7*, 252−8.

(3) Shakhgildyan, G. Y.; Lipatiev, A. S.; Fedotov, S. S.; Vetchinnikov, M. P.; Lotarev, S. V.; Sigaev, V. N. Microstructure and optical properties of tracks with precipitated silver nanoparticles and clusters inscribed by the laser irradiation in phosphate glass. *Ceram. Int.* **2021**, *47*, 14320−14329.

(4) Esposito, M.; Tasco, V.; Todisco, F.; Cuscuna, M.; Benedetti, A.; Sanvitto, D.; Passaseo, A. Triple-helical nanowires by tomographic rotatory growth for chiral photonics. *Nat. Commun.* **2015**, *6*, 6484.

(5) Chen, Y.; Yang, X.; Gao, J. 3D Janus plasmonic helical nanoapertures for polarization-encrypted data storage. *Light Sci. Appl.* **2019**, *8*, 45.

(6) Waller, E. H.; Karst, J.; von Freymann, G. Photosensitive Material Enabling Direct Fabrication of Filigree 3D Silver Microstructures via Laser-Induced Photoreduction. *Light Adv. Manuf.* **2021**, *2*, 228−233.

(7) Hossain, M. M.; Gu, M. Fabrication methods of 3D periodic metallic nano/microstructures for photonics applications. *Laser Photonics Rev.* **2014**, *8*, 233−249.

(8) Cheng, J.; Le Saux, G.; Gao, J.; Buffeteau, T.; Battie, Y.; Barois, P.; Ponsinet, V.; Delville, M. H.; Ersen, O.; Pouget, E.; Oda, R. GoldHelix: Gold Nanoparticles Forming 3D Helical Superstructures with Controlled Morphology and Strong Chiroptical Property. *ACS Nano* **2017**, *11*, 3806−3818.

(9) Famularo, N. R.; Kang, L.; Li, Z.; Zhao, T.; Knappenberger, K. L., Jr.; Keating, C. D.; Werner, D. H. Linear and nonlinear chiroptical response from individual 3D printed plasmonic and dielectric microhelices. *J. Chem. Phys.* **2020**, *153*, 154702.
(10) Galliker, P.; Schneider, J.; Eghlidi, H.; Kress, S.; Sandoghdar, V.; Poulikakos, D. Direct printing of nanostructures by electrostatic autofocussing of ink nanodroplets. *Nat. Commun.* **2012**, *3*, 890.
(11) Suryavanshi, A. P.; Yu, M.-F. Probe-based electrochemical fabrication of freestanding Cu nanowire array. *Appl. Phys. Lett.* **2006**, *88*, 083103.
(12) Seol, S. K.; Kim, D.; Lee, S.; Kim, J. H.; Chang, W. S.; Kim, J. T. Electrodeposition-based 3D Printing of Metallic Microarchitectures with Controlled Internal Structures. *Small* **2015**, *11*, 3896−902.
(13) Hirt, L.; Ihle, S.; Pan, Z.; Dorwling-Carter, L.; Reiser, A.; Wheeler, J. M.; Spolenak, R.; Voros, J.; Zambelli, T. Template-Free 3D Microprinting of Metals Using a Force-Controlled Nanopipette for Layer-by-Layer Electrodeposition. *Adv. Mater.* **2016**, *28*, 2311−5.
(14) Takai, T.; Nakao, H.; Iwata, F. Three-dimensional microfabrication using local electrophoresis deposition and a laser trapping technique. *Opt. Express* **2014**, *22*, 28109−17.
(15) Visser, C. W.; Pohl, R.; Sun, C.; Romer, G. W.; Huis in 't Veld, B.; Lohse, D. Toward 3D Printing of Pure Metals by Laser-Induced Forward Transfer. *Adv. Mater.* **2015**, *27*, 4087−92.
(16) Kuznetsov, A.; Kiyan, R.; Chichkov, B. Laser Fabrication of 2D and 3D Metal Nanoparticle Structures and Arrays. *Opt. Express* **2010**, *18*, 21198−21203.
(17) Ishikawa, A.; Tanaka, T.; Kawata, S. Improvement in the reduction of silver ions in aqueous solution using two-photon sensitive dye. *Appl. Phys. Lett.* **2006**, *89*, 113102.
(18) Tanaka, T.; Ishikawa, A.; Kawata, S. Two-photon-induced reduction of metal ions for fabricating three-dimensional electrically conductive metallic microstructure. *Appl. Phys. Lett.* **2006**, *88*, 081107.
(19) Richner, P.; Eghlidi, H.; Kress, S. J.; Schmid, M.; Norris, D. J.; Poulikakos, D. Printable Nanoscopic Metamaterial Absorbers and Images with Diffraction-Limited Resolution. *ACS Appl. Mater. Interfaces* **2016**, *8*, 11690−7.
(20) Gansel, J. K.; Thiel, M.; Rill, M. S.; Decker, M.; Bade, K.; Saile, V.; Wegener, M. *Science* **2009**, *325*, 1513−1515.
(21) Wendy Gu, X.; Greer, J. R. Ultra-strong architected Cu meso-lattices. *Extreme Mech. Lett.* **2015**, *2*, 7−14.
(22) Zeeshan, M. A.; Grisch, R.; Pellicer, E.; Sivaraman, K. M.; Peyer, K. E.; Sort, J.; Ozkale, B.; Sakar, M. S.; Nelson, B. J.; Pane, S. Hybrid helical magnetic microrobots obtained by 3D template-assisted electrodeposition. *Small* **2014**, *10*, 1284−8.
(23) Kim, S. J.; Kim, Y. I.; Lamichhane, B.; Kim, Y. H.; Lee, Y.; Cho, C. R.; Cheon, M.; Kim, J. C.; Jeong, H. Y.; Ha, T.; Kim, J.; Lee, Y. H.; Kim, S. G.; Kim, Y. M.; Jeong, S. Y. Flat-surface-assisted and self-regulated oxidation resistance of Cu(111). *Nature* **2022**, *603*, 434−438.
(24) Mun, J.; Kim, M.; Yang, Y.; Badloe, T.; Ni, J.; Chen, Y.; Qiu, C. W.; Rho, J. Electromagnetic chirality: from fundamentals to nontraditional chiroptical phenomena. *Light Sci. Appl.* **2020**, *9*, 139.
(25) Franke-Arnold, S.; Allen, L.; Padgett, M. Advances in optical angular momentum. *Laser Photonics Rev.* **2008**, *2*, 299−313.
(26) Marrucci, L.; Manzo, C.; Paparo, D. Optical spin-to-orbital angular momentum conversion in inhomogeneous anisotropic media. *Phys. Rev. Lett.* **2006**, *96*, 163905.
(27) Hassey, R.; Swain, E. J.; Hammer, N. I.; Venkataraman, D.; Barnes, M. D. *Science* **2006**, *314*, 1437−1439.
(28) Wozniak, P.; De Leon, I.; Hoflich, K.; Haverkamp, C.; Christiansen, S.; Leuchs, G.; Banzer, P. Chiroptical response of a single plasmonic nanohelix. *Opt. Express* **2018**, *26*, 19275−19293.
(29) Valev, V. K.; Baumberg, J. J.; Sibilia, C.; Verbiest, T. Chirality and chiroptical effects in plasmonic nanostructures: fundamentals, recent progress, and outlook. *Adv. Mater.* **2013**, *25*, 2517−34.
(30) Luo, Y.; Chi, C.; Jiang, M.; Li, R.; Zu, S.; Li, Y.; Fang, Z. Plasmonic Chiral Nanostructures: Chiroptical Effects and Applications. *Adv. Opt. Mater.* **2017**, *5*, 1700040.
(31) Woźniak, P.; De Leon, I.; Höflich, K.; Leuchs, G.; Banzer, P. Interaction of light carrying orbital angular momentum with a chiral dipolar scatterer. *Optica* **2019**, *6*, 961.
(32) Liu, S.; Ni, J.; Zhang, C.; Wang, X.; Cao, Y.; Wang, D.; Ji, S.; Pan, D.; Li, R.; Wu, H.; Xin, C.; Li, J.; Hu, Y.; Li, G.; Wu, D.; Chu, J. Tailoring Optical Vortical Dichroism with Stereometamaterials. *Laser Photonics Rev.* **2022**, *16*, 2100518.
(33) Ni, J.; Liu, S.; Wu, D.; Lao, Z.; Wang, Z.; Huang, K.; Ji, S.; Li, J.; Huang, Z.; Xiong, Q.; Hu, Y.; Chu, J.; Qiu, C. W. Gigantic vortical differential scattering as a monochromatic probe for multiscale chiral structures. *Proc. Natl. Acad. Sci. U.S.A.* **2021**, *118*, No. e2020055118.
(34) Ni, J.; Liu, S.; Hu, G.; Hu, Y.; Lao, Z.; Li, J.; Zhang, Q.; Wu, D.; Dong, S.; Chu, J.; Qiu, C. W. Giant Helical Dichroism of Single Chiral Nanostructures with Photonic Orbital Angular Momentum. *ACS Nano* **2021**, *15*, 2893−2900.
(35) Ouyang, X.; Xu, Y.; Xian, M.; Feng, Z.; Zhu, L.; Cao, Y.; Lan, S.; Guan, B.-O.; Qiu, C.-W.; Gu, M.; Li, X. Synthetic helical dichroism for six-dimensional optical orbital angular momentum multiplexing. *Nat. Photonics* **2021**, *15*, 901−907.
(36) Rouxel, J. R.; Rösner, B.; Karpov, D.; Bacellar, C.; Mancini, G. F.; Zinna, F.; Kinschel, D.; Cannelli, O.; Oppermann, M.; Svetina, C.; Diaz, A.; Lacour, J.; David, C.; Chergui, M. Hard X-ray helical dichroism of disordered molecular media. *Nat. Photonics* **2022**, *16*, 570−574.
(37) Daryadel, S.; Minary-Jolandan, M. Thermal stability of microscale additively manufactured copper using pulsed electrodeposition. *Mater. Lett.* **2020**, *280*, 128584.

Recommended by ACS

Engineering the Thermodynamic Stability and Metastability of Mesophases of Colloidal Bipyramids through Shape Entropy
Yein Lim, Sharon C. Glotzer, *et al.*
FEBRUARY 28, 2023
ACS NANO
READ

Multimode Vortex Lasing from Dye–TiO_2 Lattices via Bound States in the Continuum
Zhenshan Zhai, Xianyu Ao, *et al.*
JANUARY 19, 2023
ACS PHOTONICS
READ

Ultraviolet–Visible Multifunctional Vortex Metaplates by Breaking Conventional Rotational Symmetry
Nasir Mahmood, Junsuk Rho, *et al.*
JANUARY 09, 2023
NANO LETTERS
READ

Hybrid Dielectric-Plasmonic Nanoantenna with Multiresonances for Subwavelength Photon Sources
Pavel A. Dmitriev, Arseniy I. Kuznetsov, *et al.*
FEBRUARY 22, 2023
ACS PHOTONICS
READ

Get More Suggestions >

https://doi.org/10.1021/acsnano.2c10687
ACS Nano 2023, 17, 1541−1549